Simulations of Hypervelocity Impact Plasmas
OE Award No. DE-SC0022356

FINAL REPORT

Sigrid Elschot, Associate Professor
496 Lomita Mall, Durand Building Room 250, Stanford CA 94305-4035
Stanford University
(650) 725-2863
sigridc@stanford.edu

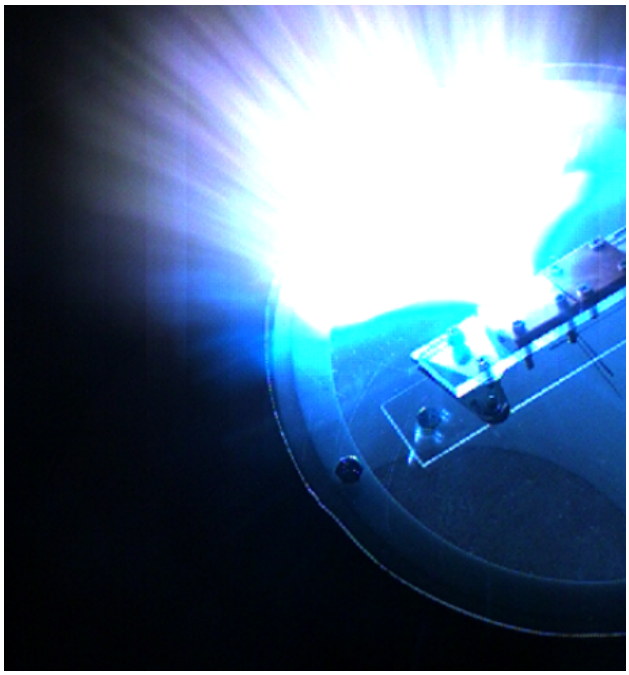

1 Introduction

The space environment is fraught with complex plasmas spanning a wide range of densities and temperatures. Much of space plasma research has focused on large-scale changes in the ambient plasma and fields from the Sun to the Earth's atmosphere, driven primarily by the solar wind. Yet one particular type of space plasma, which forms from a hypervelocity impact (HVI), remains poorly understood. Hypervelocity impactors include both meteoroids and space debris. Meteoroids are naturally occurring objects in space that travel between 11 and 72.8 km/s and originate primarily from comets and asteroids. In contrast, space debris are human-made objects with speeds typically < 11 km/s. Hypervelocity impactors routinely hit spacecraft, yet the physics behind the formation of the plasma and the dynamics of its expansion remain largely unknown. The complexity of this phenomenon necessitates a research approach that includes both experimental studies and numerical simulation in order to understand the underlying physical processes that occur upon formation and expansion of the impact plasma.

Our research has focused on providing a comprehensive understanding of plasma generated by hypervelocity impacts by meteoroids and space debris on spacecraft in order to characterize the behavior of the expanding plasma and its interactions with the ambient environment. Previously. we conducted experimental campaigns at a dust accelerator facility that can accelerate particles up to 60 km/s, which is representative of meteoroid speeds, and at a light gas gun facility that can accelerate larger projectiles up to 7 km/s, which is representative of orbital debris. The experiments included plasma, optical and radio frequency (RF) sensors in order to understand the dynamics and associated RF emission resulting from hypervelocity plasmas. For this research, we developed and applied machine learning algorithms to identify which type of impactor would produce RF and physics-based models to determine the source of the RF.

This was a one-year research program that resulted in 2 refereed journal publications (uploaded separately).

2 Background

2.1 Impactors

Meteoroids are small, naturally occurring solid bodies in space that can be rocky or ice-like, depending on their source. Meteoroids originating from comets tend to be porous and icy with a density between 0.2 g/cm^3 and 2.0 g/cm^3 while asteroidal meteoroids tend to have densities between 2.0 g/cm^3 and 7.8 g/cm^3. Meteoroids are smaller than asteroids (with the threshold ranging from 1 m to 10 m), and larger than dust (with the threshold ranging from 10 µm to 100 µm). We refer to all small, naturally occurring solid bodies including the dust population as meteoroids. In contrast, meteors are the plasma formed by a meteoroid ablating in a planetary atmosphere, and meteorites are the remnants of meteoroids that survive to impact the ground. While some meteoroid streams are associated with known parent asteroids or comets and encounter the Earth in showers at fixed dates, more comprise the sporadic meteoroids, which are the background population that can impact the Earth or spacecraft at any time of the year. Recent measurements show that the sporadic population is dominant at meteoroid sizes < 0.1 mg with typical speeds between 30 km/s and 60 km/s.

Orbital (human-made) debris is composed of objects ranging from paint chips to rocket bodies, and is primarily a threat to spacecraft in low Earth orbit (LEO). The speed of orbital debris is typically constrained below by the speed required to remain in orbit and above by Earth's escape

velocity. As a lower bound, the apogee speed of a geostationary transfer orbit starting at 200 km altitude is over 1 km/s. Earth's escape velocity from LEO is approximately 11 km/s, and circular orbital speeds in LEO are approximately 7 km/s. Orbital debris includes all the non-functioning objects derived from human activity in space. Large debris objects (on the order of 1 m or larger in size) often are generated as a result of launch- or mission-related activities, including discarded rocket stages as well as entire failed or terminated spacecraft. Smaller objects include fragmented bolts or springs from deployments and separations, objects produced in explosions or collisions, and released droplets of NaK coolant from nuclear reactors used in the Russian RORSAT series of ocean observing spacecraft. These NaK droplets form a substantial fraction of the debris population. Recent events have also caused a sudden increase in the space debris population. In 2007, Fengyun-1C was destroyed in an anti-satellite (ASAT) missile test, and in 2009, the Iridium 33 satellite collided with Kosmos 2251. These incidents, which occurred at 865 km and 789 km altitude, generated a significant amount of debris that will persist for years.

Several spacecraft have reported electrical anomalies at times of high meteoroid activity as well as in orbits that are known to have a high flux of space debris. In 1993, the Olympus spacecraft in geostationary orbit experienced several concurrent anomalies during the peak of the Perseid meteoroid shower, including a gyroscope shutdown that led to loss of attitude control and premature termination of the mission. While there was no detectable momentum transfer, the investigation into the anomalies suggested that a meteoroid impact triggered an electrical discharge. In 2009, the Landsat 5 spacecraft in low Earth orbit also experienced an attitude anomaly involving a gyroscope during the Perseid shower. In this case, attitude control and regular operation of the spacecraft was restored. For both spacecraft, it was clear that the anomalies were not due to mechanical damage because the gyroscopes were returned to operation. During the 2003 Orionid shower in October, the ADEOS-II spacecraft suffered a power failure, and during the 2011 Lyrid shower in April, the ALOS spacecraft went to a low-power mode and experienced deteriorating power generation. Both spacecraft were eventually declared total losses. Additionally, the Jason-1 spacecraft experienced random power fluctuations in 2005 in LEO after detecting a momentum transfer. The current analyses suggest that a small piece of orbital debris struck the spacecraft.

In addition to these electrical anomalies, several spacecraft have reported RF signals correlated with small (i.e. < 62 μm) hypervelocity impacts. The Cassini spacecraft detected RF signals associated with impact events from nanometer-sized particles, which had been accelerated to 450 km/s and from micron-sized particles from Saturn's rings moving at roughly 10 km/s relative to the spacecraft. Broadband electric field measurements were recorded from the 10 m dipole antennas on the Radio and Plasma Wave Science (RPWS) instrument. The STEREO pair of spacecraft have also detected electrical effects of impact events using the STEREO wave instrument (S/WAVES), which are coincident with optical measurements made by the two spacecrafts' SECCHI instrument suite.

2.2 Impact Plasma

When a hypervelocity particle impacts a spacecraft, its energy is converted into vaporization and ionization energy, fragmentation of the surface material, thermal energy within the target and ejecta, and kinetic energy of the ejecta. A fraction of the energy is converted into a shock that propagates through the material. We can estimate the total charge generated by the interaction using ground-based measurements of hypervelocity impacts on various dielectric materials, which have led to a generalized formula for charge production, given by

$$Q = 0.1m\left(\frac{m}{10^{-11}}\right)^{0.02}\left(\frac{v}{5}\right)^{3.48} \quad (1)$$

where Q is the total charge in Coulombs, m is the meteoroid mass in grams, and v is the impact speed in km/s . There are many variations of Eq. 1 published in the literature with speed exponents that range from 2.8 to 4.7. Plasma may also be multiply ionized with velocity coefficients that vary depending on primary or secondary ionization, and chemical composition of the particle may also play a role.

A difficult yet crucial parameter to estimate is the plasma density, which requires knowledge of the "size" of the plasma. A viable estimate of the initial size of the plasma is the radius at which electrons oscillate, unimpeded by collisions; this is given by the condition that the electron plasma frequency is equal to the Coulomb collision rate. This reasoning is based on the presumption that the electron and ion temperatures are tightly coupled when the collision rate exceeds the plasma frequency but may diverge once collisions become sufficiently infrequent. Such a condition represents the point where unimpeded electron oscillations may begin and allows us to estimate the temperature. Previous hypervelocity impact experiments have estimated initial temperature to be on the order of 20 to 40 eV. However, recent measurements have shown that the temperature of the plasma may be lower than 1 eV.

We may assume that the sheath becomes collisionally uncoupled from the bulk plasma and that the inherent electron oscillations are determined primarily by the local plasma frequency and bounded by the electron thermal velocity. When the plasma has diluted to the point where the electron-ion collision frequency is approximately equal to the plasma frequency, the surface electrons can effectively separate from the background ions and produce coherent radiation at the plasma frequency. Depending on space environment conditions, a spacecraft may also produce an external electric field that drives the electrons and separates the species. The extent of the separation is approximately one Debye length, which depends on the local density and temperature. At this stage, the plasma expands freely, which lowers the density and the effective peak emission frequency. A schematic representation of the expanding plasma is shown in Figure 1.

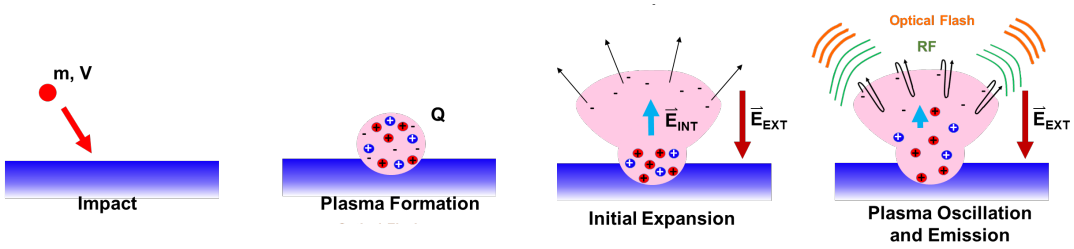

Figure 1. Hypervelocity impact flash and plasma model. A particle impacts the spacecraft, producing a plasma with total charge Q that then expands into the vacuum. As the resulting plasma expands outward, the external electric field E_{ext} due to surface charging of the spacecraft will accelerate the electrons out first and cause a charge separation. An internal electric field E_{int} is thus created. Plasma oscillations will result from the competition between E_{int} and E_{ext}, and generate RF/optical emission.

3 Research

3.1 Charge Production

We collected data in a series of experiments conducted in 2011 using the Van de Graaff dust accelerator at the Max Planck Institute for Nuclear Physics. A total of 6529 impact events were observed inside a 1.4 m test chamber, maintained at pressures between 3.0 × 10−6 mbar and 1.0 × 10−5 mbar. This pressure range provided vacuum conditions and established a mean free path longer than the chamber diameter, which allowed for the collisionless and free expansion of the impact plasma. Spherical iron particles with a mass range from 10−16g to 10−11g and an initial speed range from 3 km/s to 66 km/s were used as impactors on different target materials, which represented a variety of spacecraft surfaces. Targets included tungsten, aluminum, solar panel substrate, two optical solar reflectors, and two solar cells, one with uncoated cover glass in a LEO (Low Earth Orbit) configuration and another with conductive coating in a GEO configuration. In addition, multiple variations of active targets which used an electric field antenna (E field sensor) as the target surface were used. Note that these impact events produced micrometer craters, with a fully vaporized plume of gas and plasma. However, impacts can also produce a large amount of initially neutral macro-ejecta or dust, which can greatly affect the properties of the plasma. Figure 2 shows the projectile mass and velocity distribution for these impacts, color coded by target voltage. Note that these impact events cover a wide range of mass and velocity values.

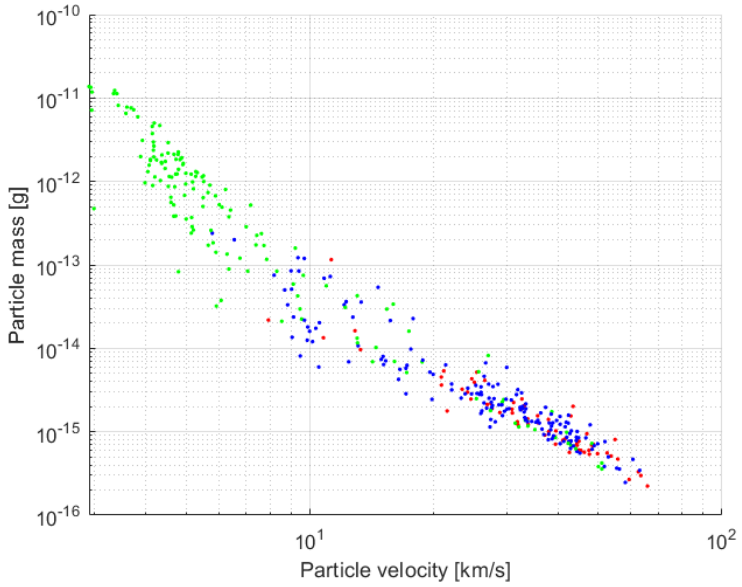

Figure 2. Projectile mass and velocity distribution for 100V (red), -100V (blue), and -300V (green) target bias.

Multiple sensors were designed and used in the experiment to observe different aspects of the impact event, including the following: 1. A photomultiplier tube to characterize the optical emission, which provides the impact timing. 2. Six patch antennas tuned to 315MHz and 916MHz to observe the radio frequency (RF) emission. 3. Two retarding potential analyzers (RPA) to measure the current produced by the expanding plasma. The two RPA sensors, shown in Figure 3, were placed in front of the impact point at distances of 65±1mm and 85±1mm from the target surface normal vector. Note that because of its greater sensitivity to the expanding plasma plume, measurements from the nearer RPA were used for this study.

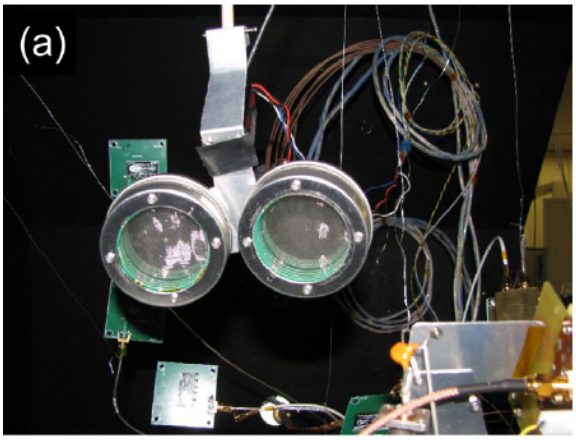

Figure 3. RPA sensors.

To investigate the charge production (Eq. 1) we analyzed data from the RPA (shown in Figure 3). Since multiple ion species with different masses can be created upon the impact, there can be multiple peaks on the RPA output voltage, where each peak represents a different species. Lighter species achieve higher velocities and reach the sensor faster and to form the initial peaks, whereas the heavier ones reach the sensor later and form the secondary peaks. For this study, we only looked at the impact events with two distinguishable peaks, which represent production of two different species upon the impact. Figure 4 (left) shows an example of an impact event on LEO target with three peaks, which was not used for this study). This reduced the total number of measurements from 367 to 192.

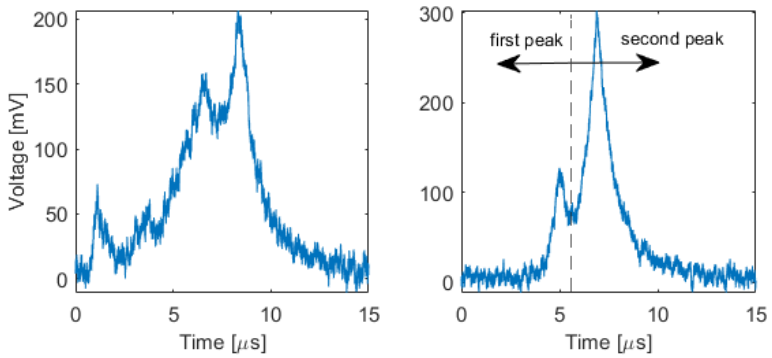

Figure 4. Left: example of an impact event on a LEO target, showing production of three different species (target bias = 100V). Right: Cutoff line to separate the first and second peaks

The transfer function of the transimpedance amplifier used in the RPA sensor (GRPA) is determined by measuring the frequency response of this sensor to a test input signal or

$$G_{RPA}(s) = \frac{4\times10^{20}s}{(50+s)\left(1.78\times10^{6}+s\right)\left(1.68\times10^{7}+s\right)} \quad \frac{V}{A}$$

where the voltage is in volts (V), current is in amperes (A) and s represents the Laplace transform domain. A best fit function to each peak of the voltage data is found with MATLAB using the non-linear least square method. The mathematical form of this function in Laplace domain is then substituted in Equation 3 to find the current, I. Note that V(s) has to be in such a form that after multiplying it by the inverse of the RPA transfer function, GRPAs, gives a causal current in Laplace domain, I(s). Causal systems have a greater number of poles than zeros, meaning that their output only depends on the past and current input and not on the future input. Considering this criterion, the function Vt= atebt+c is found as an acceptable fit to the output voltage data. The Laplace transform of this fit is

$$V(s) = \frac{a}{(s-b)^2} + \frac{c}{s}$$

which guarantees a causal current after multiplication with the inverse RPA transfer function. The coefficients of V(t) for each peak of each impact event are calculated in MATLAB using iterative least squares estimation.

The method described above was applied to each peak for the impact events under consideration. Figure 5 shows this technique applied to the second peak of an impact event with a target bias of +100V. As can be seen, the data is divided into three sections: blue, green, and yellow. Two different functions were fitted to the blue and yellow data points. To resolve fitting discontinuities at the peak, where the two fits approach each other, a quadratic fit was used around the green portion of the data. This portion was chosen to be 300 data points (0.12 μs) after and before and after the point with the highest voltage value. Note that this quadratic fit also maintains the causality of the system

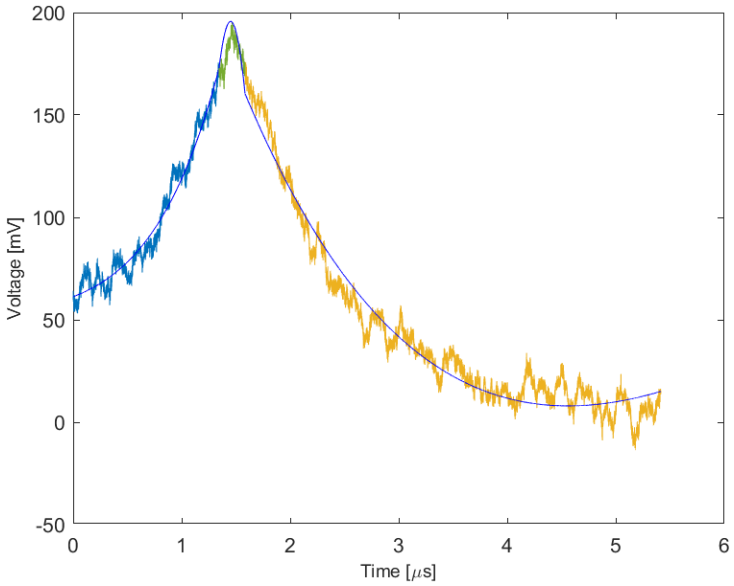

Figure 5. Fits to the blue and yellow portions of the data. Quadratic fit was used on the green portion to resolve fitting discontinuities.

To find the total impact charge produced (Q), we integrate the current, I(t), with respect to time. Its value is then substituted in Equation 1 to find the velocity power for each peak at each impact event. Since the velocity and mass of the impactor for each event is known, the only unknown in the Equation is the velocity power, β. Figure 6 illustrates how β is evaluated, at everyfor each target bias. Note that to find the β for each case, we took the logarithm of Equation 1 and found the best linear fit to theQ vs. log v data. The slope of this linear fit is β. Plots also include a 95% interval error around the best fit which is an indication of how accurate the calculated velocity powers are. In addition, Table 1 contains the numerical β values for each peak and for each target bias voltage, and their corresponding numerical 95% interval errors.

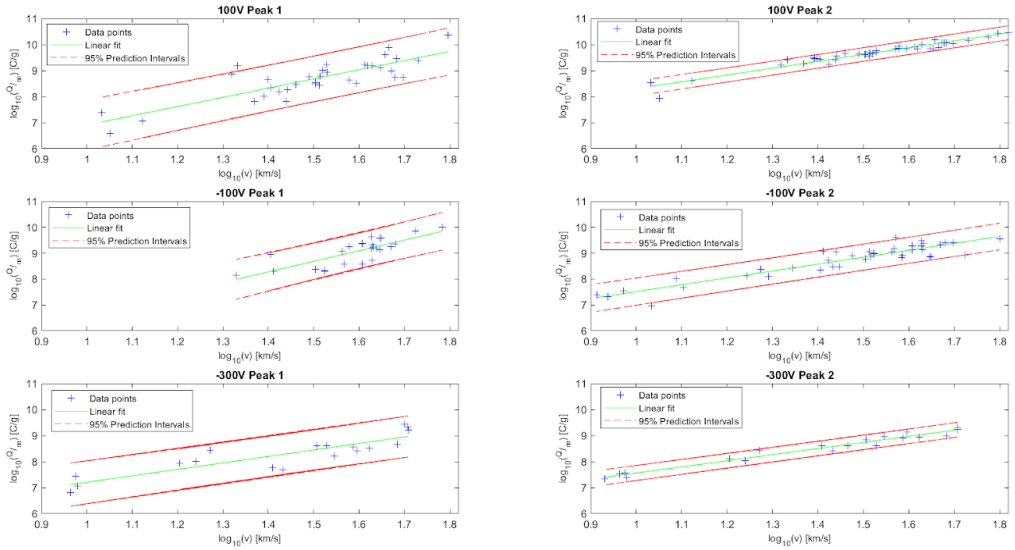

Figure 6. Plot of Q vs. log v of each peak, at each target bias. The slope of the best linear fit to these data points is the velocity power, β.

Table 31 Velocity power for the first and second peak of each target bias configuration.

Target voltage (V)	Peak 1	Peak 2
100	3.53 ± 0.82	2.61 ± 0.23
-100	4.09 ± 1.35	2.66 ± 0.35
-300	2.48 ± 0.69	2.35 ± 0.23

3.2 Particle-in-cell Simulation

The DG-PIC scheme contains three main components: (i) the discontinuous Galerkin (DG) scheme to calculate the electric and magnetic field, ***E*** and ***B***, respectively, (ii) the PIC scheme to model the charged species dynamics and to calculate the source terms for the DG scheme, and (iii) the

Coulomb collision models. The DG method is a useful scheme for modeling wave phenomena on an unstructured mesh; it is able to obtain high-order accuracy solutions within each element (similar to the finite element method) while allowing for local wave behavior to propagate (similar to the finite volume method). Furthermore, it prevents numerical Cherenkov radiation due to the convex nature of the dispersion relation of the scheme and has attractive stability properties. The main addition in this work to the DG-PIC model developed by Fletcher and Close is the addition of Coulomb collisions to better model electron and ion separation within the bulk. We employ two different models: a small-angle Coulomb collision model and a general Coulomb collision. Both Coulomb collision models have the same basic steps. For a Coulomb collision, there is a given target particle that is affected by the Coulomb force of an ensemble of field particles within a given computational cell. The Coulomb scattering process is described in the following procedure.

1. Given an ensemble of field particles, calculate the bulk velocity of the field particles, $\boldsymbol{v}_f$.
2. Given a target particle velocity $\boldsymbol{v}_t$, shift the velocity to a reference frame such that the bulk velocity is zero, i.e., $\boldsymbol{w} = v_{\boldsymbol{t}} - v_{\boldsymbol{f}}$, where $\boldsymbol{w}$ is the target particle velocity in the new reference frame.
3. Rotate the lab frame axes $\hat{\boldsymbol{x}} - \hat{\boldsymbol{y}} - \hat{\boldsymbol{z}}$ by angles θ and ϕ such that in the $\hat{\boldsymbol{x}}' - \hat{\boldsymbol{y}}' - \hat{\boldsymbol{z}}'$ coordinate system, $\boldsymbol{w}$ is parallel to the $\hat{\boldsymbol{z}}'$ axis via Euler angle rotations.
4. Stretch the target particle velocity vector by magnitude Δw and scatter the velocity vector by angles $\Delta\alpha$ and $\Delta\beta$.
5. Rotate back to the original lab frame axes $\hat{\boldsymbol{x}} - \hat{\boldsymbol{y}} - \hat{\boldsymbol{z}}$.
6. Apply energy correction factors to conserve energy and momentum.

This procedure is repeated for every species. The difference between scattering models lies in step 4 in the calculation of the scattering angles $\Delta\theta$ and $\Delta\phi$ and the increase in speed Δw.

The test problem being considered is a conical plasma in the center of the computational domain with open/absorptive boundaries on every side, as shown in Figure 7. This is a simplifying assumption, as true hypervelocity plasmas have a nearby charged spacecraft boundary. Not only would these boundaries exert a background electric field on the plasma, but the material properties of the spacecraft would affect how the radiation is reflected onto the expanding plume. Furthermore, geometrical effects due to craters formed during impact may be significant. These effects will be investigated in a future work. The computational domain spans from $x \in [-9,9]$ μm and $y \in [-5,13]$ μm to measure free space radiation. A subset of this computational domain is shown in the results for clarity and to neglect residual boundary effects. The unstructured mesh is composed of approximately 21,000 fourth-order elements of relatively uniform spacing. Future work will take advantage of the model's meshing capabilities to investigate geometric effects cause by impact craters. Figure 8 shows the charge density, electric fields, and magnetic field at times $t = 1.05 \times 10^{-14}, 2.10 \times 10^{-14}$, and 3.15×10^{-15} s, or times corresponding to $2.4/\omega_p$, $4.8/\omega_p$, and $7.2/\omega_p$, respectively. These time samples correspond to the first, second, and third columns, respectively. At time $t = 1.05 \times 10^{-14}$ s, there are both electrostatic waves within the conical plasma and electromagnetic waves propagating perpendicular to it. After a few periods, electrostatic waves begin to stabilize within the conical plasma. This can be best seen by the striations in the charge density; striations in the E_x and E_y fields are also visible.

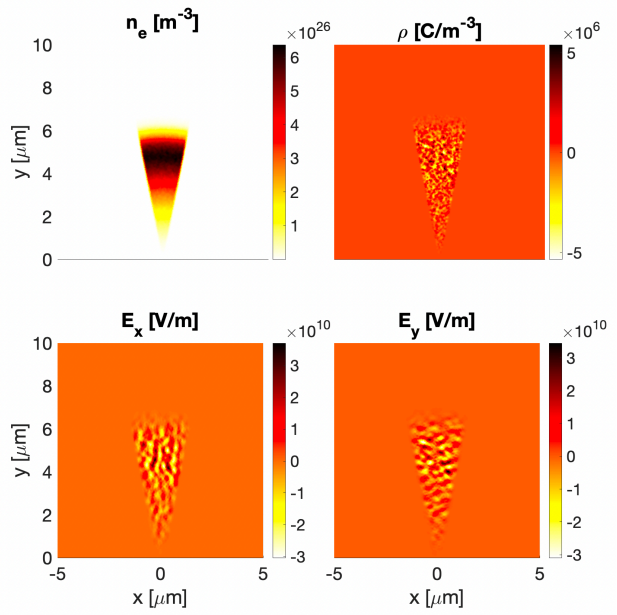

Figure 7. Initial plasma conditions for the electron number density n_e, charge density ρ, and electric fields E_x AND E_y. Note the peak plasma density at a radius of 4.75 μm, which is done to simulate the results of Fletcher [2].

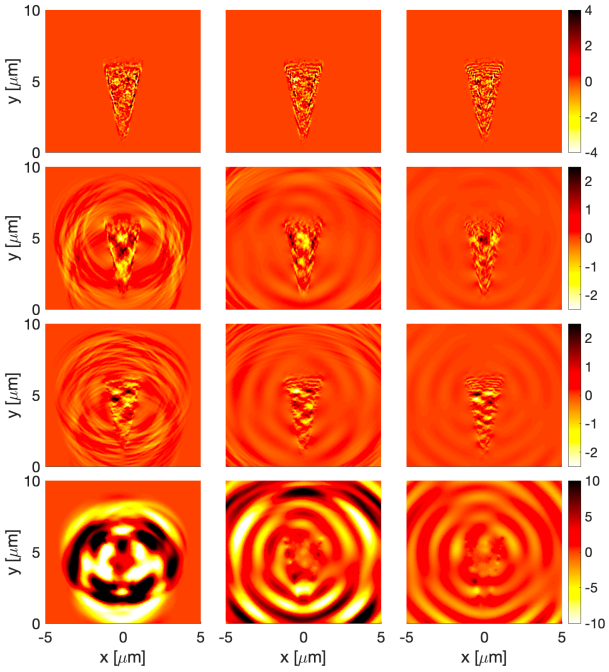

Figure 8. Charge density ρ in 10^6 C/m^3 (first row), electric fields E_x (second row) and E_y (third row) in 10^{10} V/m, and magnetic field B_z (bottom row) in T. Each column shows a snapshot at time $t = 1.05 \times 10^{-14}$ s (left), $t = 2.10 \times 10^{-14}$ s (middle), and $t = 3.15 \times 10^{-14}$ s (bottom), which correspond to $2.4\omega_p$, $4.8\omega_p$, and $7.2\omega_p$.

4 Summary

We developed a new technique for finding the charge production power law in hypervelocity impact of iron projectiles on LEO target with bias configurations of 100, -100 and -300V, and have modified our existing PIC. Results show that in negative bias cases, electrons have a different power law compared to SiO2-. In addition, the power law is bias dependent for electron formation whereas it doesn't depend on bias for SiO2- formation. We also found that the negative peaks come from electron attachment associated with an ionization mechanism whereas the positive peak requires a dissociation mechanism to occur. These results indicate that the plasma formation from HVI can be simultaneously governed by multiple power laws for different species, and that the overall composition of a HVI plasma would therefore depend on the impact speed. For the simulations, electromagnetic pulse generation is reliably reproduced with collisionless and collisional charge separation. Coulomb collisions cause a decrease in frequency along with increased heating within the plasma, as electromagnetic energy is redirected towards scattering in the *z* direction, mimicking 3D relieving effects.